

Analysis and simulations of droplet generation regimes in a coaxial microfluidic device

Alessio Innocenti*, Andrea Poggi, Simone Camarri, Maria Vittoria Salvetti

University of Pisa, Dipartimento di Ingegneria Civile e Industriale, Largo Lucio Lazzarino, 56122, Pisa, Italy

Abstract

The generation of microdroplets via segmentation in microfluidic devices is of interest in many applications, from biochemical to pharmaceutical. This technique permits indeed much higher control on the droplet size, uniformity and generation rate than in standard batch generation processes. In this work we have evaluated the suitability of the open-source software Basilisk to accurately predict microdroplet generation by segmentation. We have validated the numerical tool with analytical solutions for the dynamics of droplets in confined flows, namely with Bretherton theory, and by comparison with literature experimental results. We have then performed several campaigns of numerical simulations for a coaxial device, analyzing the different regimes of droplet generation, and evaluating how the physical and flow parameters affect the production mechanisms and the diameters of the generated droplets. Finally we have proposed new scaling laws for the prediction of droplet diameters in the dripping and jetting regimes, refining existing ones by taking

*Corresponding author

Email address: `alessio.innocenti@unipi.it` (Alessio Innocenti)

into account additional physical effects, like the viscosity ratio.

1. Introduction

The processes of droplet generation at the milli to micro scale has attracted considerable attention due to the numerous applications in which micro-droplets are involved, such as: (i) lab-on-a-chip devices (miniaturized reproductions of laboratory processes at the micro/milli scale) for sample preparation, mixing, separation and detection; (ii) drug delivery through microparticles, nanoparticles, coated microparticles and microencapsulation, which has the great advantage of delivering small doses of drug only in the desired site, reducing accumulation and undesired systemic effects, together with a better control on the release rate, by modifying the microenvironment [1]; (iii) encapsulation and manipulations of single cells in aqueous droplets for cell culture, which allows isolating each individual cell in its microenvironment [2]. Droplet generation via segmentation in microfluidic devices has the great advantage with respect to batch methods of ensuring excellent control on size distribution, allowing the generation of almost monodisperse droplets, and on generation rates, at the cost of lower processed volumes. The generation of microdroplets via segmentation is generally achieved at a junction of separate channels fed with immiscible fluids, generally oil and an aqueous solution, through different possible regimes, namely squeezing, dripping and jetting [3]. The analysis of different design configurations, geometries and response to variations of physical parameters is crucial for the optimization of the devices and to maintain the control, first of all on the production regime, secondly on droplet volume, production rates and monodispersity.

The geometrical configurations can range from cross-flow and T-junction, to co-flow, and flow focusing setups. The balance of the forces driving the breakup instability are surface tension, which has a stabilizing effect, on one side, and viscous stresses from the outer fluid and inertial forces of the inner fluid, which have destabilizing effects, on the other side. This balance can be quantified through the dimensionless Capillary and Weber numbers. At very low capillary number the stabilizing effect of surface tension can largely overcome viscous stresses, therefore at the junction the jet tip of the dispersed phase grows until it fully obstructs the junction, causing a sudden increase in the upstream pressure which causes the necking and the breakup of the jet. At larger capillary numbers, the system can reach the marginal equilibrium of forces, leading steadily to the dripping regime, or it can undergo a convective instability driven by the RayleighPlateau instability of the jet interface, leading to the jetting regime. The different regimes of formation and the underlying physics have been largely studied, extensively in experimental literature [4, 5, 6], more recently also with numerical approaches, which have the advantages of more flexibility of use, lower costs and easier inspection of physical fields. However, even if the fluid dynamics of such devices is simple at first sight, given the very low Reynolds numbers involved, which implies that the flows are inherently laminar and can generally be described by the Stokes equations, interfaces can complicate the numerical solution significantly, leading to possible lack of accuracy if not properly handled, or in the worst case to numerical instabilities, due to the amplification of capillary waves. This latter complication, with an explicit treatment of surface tension, can only be overcome at the expense of using very small time steps,

which greatly increases computational costs. Even if not always all these aspect are considered rigorously, the literature on numerical approaches to droplet generation in microdevices is rapidly increasing, and different methods and softwares are now commonly used in device design. Hua *et al.* [7] have simulated coflowing devices with a front-tracking method [8] to track the interface between the two immiscible phases, exploiting mainly the dripping and jetting regimes at different values of the Capillary and Weber numbers. De Menech *et al.* [9] have analyzed the transition from squeezing to dripping in a T-junction with the phase-field method, which adopts a diffuse interface approach, justified by the low capillary numbers (dominant effect of surface tension) in microfluidics, and relating the breakup dynamics to the upstream pressure variations. Wu *et al.* [10] have performed three dimensional simulations with the lattice Boltzmann method for a cross-junction configuration, with a surface tension calculation based on the continuum surface force (CSF) method, with a good comparison with experiments. Afkhami and coworkers have explored the use of Volume-of-Fluid (VOF) methods for the interface tracking, together with the geometrical height function method for the calculation of curvature and the estimation of surface tension, in a T-junction [11] and in a co-flowing configuration in a Hele-Shaw cell [12]. A different VOF implementation has been adopted in another work [13] to study the effect of the injection angle in a 3-dimensional cross-flow geometry, while the most widely used numerical tool for such kind of flows probably remains OpenFOAM with its *interFoam* solver, which is still based on the VOF method, but with a diffuse interface approach [14, 15, 16]. It is worth mentioning that, in parallel, research is also being conducted using commercial codes,

such as ANSYS Fluent, where a VOF implementation is present as well [17].

The literature on numerical approaches to microfluidics is, therefore, very heterogeneous, without a method being completely affirmed with respect to the others. In this work we want to evaluate the suitability of the open-source software Basilisk (<https://basilisk.fr>) to tackle those kind of applications. Recently, Harispe et al. [18] have adopted Basilisk to evaluate its applicability to droplet generation in coaxial and T-junction configurations with encouraging results, although only for a limited range of configurations and parameters. Our intent is, therefore, to investigate deeper some peculiar numerical aspects of Basilisk in the application to droplet generation in microdevices, assessing its accuracy against theoretical and experimental results, and exploiting its usage for droplets regime production and diameter predictions. We then analyze droplet generation regimes in a coaxial device and the influence of physical and flow parameters. New scaling laws are finally proposed to predict droplet diameters in the dripping and jetting regimes, improving existing ones by including additional effects such as the viscosity ratio.

The work is structured as follows: in Section 2 we briefly describe the mathematical formulation of the problem; in Section 3 we report the details of the numerical implementation of Basilisk; in Section 4 we validate and assess the accuracy of Basilisk for a Taylor bubble configuration; in Section 5 we analyze in details a coaxial configuration for droplet generation with validation against literature experiments, regime mapping and derivation of scaling laws for the droplet diameter.

2. Modeling and governing equations

We describe the dynamics of droplet generation in a microfluidic device, where two non-miscible fluids enter from separate channels, come in contact at a junction, and flow out from the same channel. The physical parameters characterizing the problem are the viscosities and densities of the two fluids, μ_i and ρ_i , and surface tension σ . The index i denotes the continuous, c , or the dispersed, d , phase. Once the geometry is fixed (e.g. coaxial, cross junction, etc.), the additional parameters characterizing the flow are the inlet velocities of the two fluids, U_c and U_d , and a characteristic dimension of the channels, typically the diameter, D , in coaxial configurations or the channel height, H , in square section channels. Based on these physical, geometrical and flow parameters, four dimensionless groups can be formed: firstly the viscosity and density ratios, respectively μ_d/μ_c and ρ_d/ρ_c ; secondly the Reynolds and Capillary number, that for these kind of flows can be defined based on the continuous phase properties as follows

$$Re_c = \frac{\rho_c U_c D}{\mu_c}, \quad Ca_c = \frac{\mu_c U_c}{\sigma} \quad (1)$$

An alternative, quite common in microfluidics literature, is to replace one of these two dimensionless number with the Weber number, defined as follows:

$$We_c = \frac{\rho_c U_c^2 D}{\sigma} = Re_c \cdot Ca_c \quad (2)$$

The two fluids are governed by the Navier-Stokes incompressible equations with variable density and viscosity, which in their dimensionless form

are as follows:

$$\nabla \cdot \mathbf{u} = 0 \quad (3)$$

$$\varphi_r \left(\frac{\partial \mathbf{u}}{\partial t} + \mathbf{u} \cdot \nabla \mathbf{u} \right) = -\nabla p + \frac{1}{Re_c} \nabla \cdot (2\lambda_r \mathbf{D}) + \frac{1}{Re_c} \frac{1}{Ca_c} \kappa \mathbf{n} \delta_s. \quad (4)$$

$\mathbf{D} = [\nabla u + (\nabla u)^T]/2$ is the symmetric strain-rate; $\varphi_r = \rho(\mathbf{x}, t)/\rho_c$ is a dimensionless density; $\lambda_r = \mu(\mathbf{x}, t)/\mu_c$ is a dimensionless viscosity. The last term represents a non-dimensional surface tension with κ and \mathbf{n} being the local curvature and the interface unit normal, and δ_s representing a Dirac delta function that is non-zero only at the interface. We do not consider variable surface tension over the interface separating the two fluids.

The volume fraction C is used to distinguish between the different phases, being $C = 1$ in the continuous phase, $C = 0$ in the dispersed one, and $0 < C < 1$ at the interface. This scalar field is advected by the equation:

$$\frac{\partial}{\partial t} C + \mathbf{u} \cdot \nabla C = 0, \quad (5)$$

The variable density and viscosity are evaluated weighting the continuous and the dispersed contribution with the local volume fraction as follows:

$$\rho(\mathbf{x}, t) = C\rho_c + (1 - C)\rho_d, \quad \mu(\mathbf{x}, t) = C\mu_c + (1 - C)\mu_d, \quad (6)$$

This set of equations is numerically solved with Basilisk.

3. Numerical implementation

Basilisk (<http://basilisk.fr>) is a library of solvers that can be used for a variety of fluid dynamics applications, from industrial to geophysical flows. Basic solvers and functions can be included in a script in order to

build a specific solver assembly with the desired features. All the different parts share a common discretization based on the finite volume method on Cartesian grid. The grid can also be dynamically refined or coarsened based on specific criteria and relying on a quadtree (2-d) or octree (3-d) refinement strategy [19]. In this work we rely on the Navier Stokes centered formulation, where the spatial discretization is done with a finite volume centered method, while temporal discretization is carried out by means of a second-order fractional-step method with a staggered discretization in time of the velocity and scalar fields [19], relying on the Bell-Colella-Glaz second-order unsplit upwind scheme for the estimation of the advection term [20]. The Poisson equation is solved iteratively using an efficient multilevel solver constructed on the quad/octree grid. More details can be found at <http://basilisk.fr>. All simulations performed with Basilisk have been done with adaptive mesh refinement (AMR) on quadtree grids.

The interface is advected with a geometric piecewise-linear interface construction (PLIC) VOF method ([21, 22]), generalized for the quad/octree spatial discretization, which can ensure a sharp interface while preserving mass conservation. The scheme is made of two steps: (i) first the interface is geometrically reconstructed, (ii) then the fluxes are evaluated and interface is advected. In the PLIC method the interface is approximated by a local segment of equation $\mathbf{m} \cdot \mathbf{x} = \alpha$. The normal \mathbf{m} is determined with the volume fraction in the cell and in the neighbouring ones using the Mixed-Youngs-Centered scheme [23]. Then, the interface line is moved along the normal by changing α to obtain the desired volume fraction. The advection equation is then integrated using dimension-splitting, which solves along each dimen-

sion successively, with a fractional step method that guarantees exact mass conservation.

The surface tension term in Equation (4) is modeled with the continuum surface force (CSF) approach [24]. Accurate computation of the curvature is carried out using the height-function method [19].

The device geometry is defined in Basilisk through the embedded boundary method (EBM), originally proposed in [25, 26], and widely used in Basilisk literature for moving boundaries [27], solidification modelling [28], and two-phase flows with complex geometries [29]. The method embeds a sharp representation of a solid surface on a regular Cartesian grid. The reconstruction of the solid interface is done using a piecewise linear reconstruction, using a signed distance function sampled on the vertices of the Cartesian grid for the geometrical properties. The discrete operators in the cut cell are then properly defined with the finite volume method with 2nd order accuracy [29] for single phase flow / 1st order accuracy when coupled with the VOF method.

Concerning the boundary condition of the fluid volume fraction at the cut cell, a particular treatment must be adopted when in the same cell there are the two liquid phases and the solid, indeed a condition on the contact angle need to be set [30, 31]. For more details on the numerical implementation of the contact angle condition in Basilisk, see [29]. In all the present simulations, when the contact between the interface and the wall is present, we have used an equilibrium contact angle of $\alpha_w = 30^\circ$ (measured between the wall and the interface in the continuous phase), which is within the typical range of values adopted in numerical simulations [17, 16, 15]. A precise tuning of the value

of the equilibrium contact angle, which depends on the specific properties of the fluid and of the solid surface, was not carried out, as it would require a more detailed characterization of the experimental conditions, which is beyond the scope of the present work, as the comparison is performed with an experiment from the literature.

For the velocity and pressure fields we set an inlet boundary condition with constant velocity at the entrance of the channel, a no-slip condition at the walls, and an outflow condition with fixed pressure at the outlet of the channel. In the axially symmetric configuration we set axial symmetry on the symmetry axis, which is located at the bottom of the domain ($y = 0$). More details on geometries and boundary conditions are given in the following sections.

4. 2-dimensional Taylor bubble

Before studying the droplet generation in a coaxial device, we assess the accuracy of Basilisk in reproducing the dynamics of a Taylor bubble, since the literature on Basilisk applications to problems with bubbles/droplets in microchannels is still very limited to date. In particular we analyze a 2-dimensional configuration with an already formed droplet/bubble in a straight channel at small values of Re and Ca numbers. We try to reproduce the results of Fullana *et al.* [32], a precursor work focused on Gerris code (a former version of Basilisk). The geometry consists therefore in a straight channel of height H with an already formed droplet of initial ellipsoidal shape, with equivalent diameter larger than the channel height. A constant inlet velocity is used as boundary condition on one side of the channel, while an outflow boundary condition is used on the other side, with no-slip at the

walls. After a transient where the droplet deforms and accelerates, a steady shape and velocity are reached within fractions of diameter downstream of the initial position. The Reynolds number is kept fixed with a value of $Re = 0.1$, while the Capillary number is varied in the range $Ca = [0.0005 - 0.1]$. The density and viscosity ratios are kept constant and unitary, i.e. $\rho_d/\rho_c = 1$, $\mu_d/\mu_c = 1$.

The adaptivity criteria of the grid have been set on the two components of velocity, solid fraction and VOF volume fraction, with the respective thresholds defined as follows: $\epsilon_{u_x} = \epsilon_{u_y} = 0.007$, $\epsilon_{cs} = 10^{-3}$, $\epsilon_f = 10^{-1}$. Indeed, as can be seen in Figure 1, which shows an example of grid resolution and adaptivity for two different cases of Capillary numbers, the refinement is effective at the interface, at the solid wall, and at the rear of the droplet where the distance between the interface and the wall is smaller and the gap velocity is therefore higher.

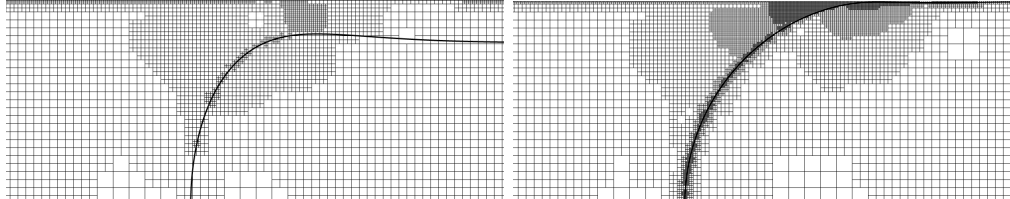


Figure 1: Example of grid adaptivity for the Taylor bubble at $Re = 0.1$. Left panel $Ca = 0.1$, maximum resolution $H/\Delta = 204$, right panel $Ca = 0.001$, maximum resolution $H/\Delta = 410$.

We compare our results with the analytical solution of Bretherton theory [33, 32], which gives the film thickness, t , between the droplet and the wall, as a function of the Capillary number as follows:

$$\frac{2t}{H} = 0.643(3Ca)^{2/3} , \quad (7)$$

and with the semi-empirical relation of Aussillous et al. [34], which goes beyond the limit of very small Capillary number, and yields:

$$\frac{2t}{H} = \frac{0.643(3Ca)^{2/3}}{1 + 0.643 \cdot 2.50 \cdot (3Ca)^{2/3}}. \quad (8)$$

From both relations we can then derive the droplet dimensionless velocity, applying those results to a Poiseuille flow [15]:

$$\frac{U_d}{U_f} = \frac{1}{1 - 2t/H}, \quad (9)$$

We evaluate the droplet velocity by volume averaging the velocity field over the whole inside of the droplet and we compare then the average droplet velocity with Equation 9.

Small Capillary numbers, as those typical of microfluidics and of this study, results in thin gaps between the droplet and the wall, and correctly resolving that region with a sufficient grid resolution is crucial in identifying the droplet shape and in turn its terminal velocity. For this reason we have performed, for the case with $Ca = 0.001$, a series of convergence tests on the most relevant numerical parameters: (i) the grid maximum level of refinement; (ii) the thresholds used to dynamically refine/coarse the grid; (iii) the tolerance used in the successive multigrid resolution of the Poisson equation. The maximum refinement level has been varied in the range $LEV = [8 - 12]$, resulting in a maximum grid resolution in the range $H/\Delta = [25 - 410]$, with a total number of cells at steady state of $N \simeq 4 \cdot 10^4$ for $H/\Delta \simeq 100$; $N \simeq 6 \cdot 10^4$ for $H/\Delta \simeq 200$; $N \simeq 9.8 \cdot 10^4$ for $H/\Delta \simeq 400$. Figure 2(a) shows the droplet velocity with the different grid resolution. It is clear that a resolution between $H/\Delta = 100 - 200$ is necessary, therefore for the other simulations we will adopt a grid resolution of $H/\Delta \simeq 200$ (except for the smallest $Ca = 0.0005$

for which we have refined up to $H/\Delta \simeq 410$). We have then analyzed the effect of varying the adaptivity thresholds to refine or coarse the grid. We have found no significant variations of the results by varying the criteria for the solid embedded fraction (cs) and the volume fraction (f), which are not reported here for the sake of brevity. The effect of the adaptivity threshold for velocity has been analyzed in the range $\epsilon_{u_x} = \epsilon_{u_y} = 10^{-2} - 10^{-3}$, showing negligible variations of the droplet velocity, as it can be seen in Figure 2(a).

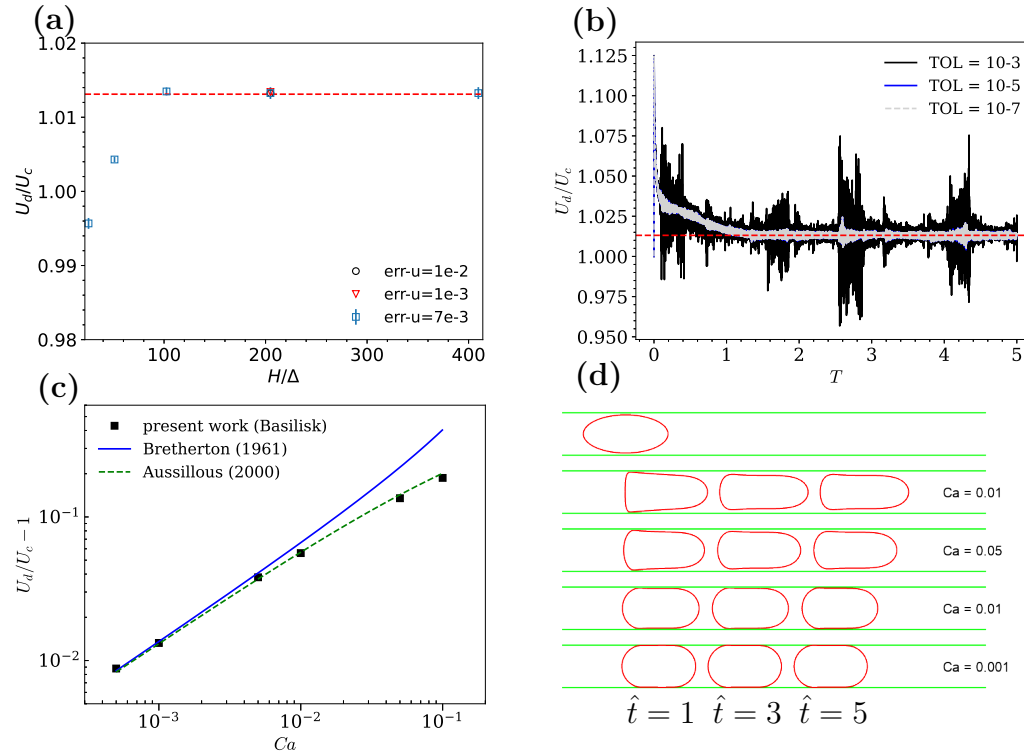


Figure 2: (a) Grid convergence for $Ca = 0.001$ and $Re = 0.1$: droplet terminal velocity at different grid resolution and for different adaptivity thresholds. The red line represents the steady state value obtained with the semi-empirical relations [34]. (b) Temporal evolution of the droplet terminal velocity with different tolerance for the multigrid Poisson equation resolution. (c) Droplet terminal velocity at different Capillary numbers compared to Bretherton theory [33] and literature semi-empirical relations [34]. (d) Droplet shapes for different Capillary numbers, at different times.

The tolerance parameter of the multigrid poisson solver needs also to be properly tuned to avoid numerical instabilities. Indeed, the very small Reynolds and Capillary numbers, imply extremely small time step, due to the explicit treatment of surface tension [19], and in turn the tolerance of the Poisson equation resolution might need to be varied with respect to the default value. Figure 2(b) shows the temporal evolution of the droplet velocity with different tolerance values. The large fluctuations observed with too high values, are largely reduced with lower values, and from $TOL = 10^{-5}$ results are fully converged.

Finally, Figure 2(c) shows the dimensionless droplet velocity for different Capillary numbers, compared with Equations 7-9. Results are in excellent agreement with the empirical relation of Aussillous et al. [34], especially for the lower Capillary numbers, while for $Ca = 0.1$ we reach a maximum error of $\sim 6\%$. A qualitative description of droplet shapes at different Capillary numbers is shown in Figure 2(d), at three different instants. The shape changes significantly from the classic Bretherton shape to a more symmetric flattened “pancake” like shape at very low Capillary numbers.

5. Coaxial droplet generator

The coaxial configuration analyzed is the one described by [35], in which the inlet duct for the dispersed phase has an inner diameter $d_{in} = 0.16mm$ and an outer diameter $d_{out} = 0.31mm$, while the inlet duct for the continuous phase has diameter $D = 0.51mm$. The total length of the simulation domain is $L = 20D$, while the inner duct extends up to $L_{in} = 3D$. The initial position of the interface separating the two phases is a straight line at $x = 2.8D$, perpendicular to the walls of the inner duct.



Figure 3: Sketch of the coaxial device.

The continuous phase consists of silicone oil of various viscosities (denoted as SO- μ , where μ is expressed in [$mPas$]), while the dispersed phase is a polysulphone solution (PSF) at various concentrations, thus varying the viscosity and slightly the density (which is nevertheless considered constant). Physical properties are reported in Table 1 below.

	SO50	SO100	PSF 6%	PSF 8%	PSF 10%
$\mu[mPa \cdot s]$	50	100	9.23	22.7	46.2
$\rho[kg/m^3]$	979	979	969	979	991

Table 1: Physical parameters.

Before running the complete set of simulations for different combinations of SO and PSF, varying the fluid flow rates to change the dimensionless parameters, we did a preliminary visual validation based on two standard configurations considered in Lans article [35], representing the two main flow regimes: drop-flow and jet flow. We set up accordingly the simulations with the same flow rates as in Lans work, shown in Table 2 below, and adopted a maximum grid resolution of $D/\Delta = 102$.

	ρ_c/ρ_d	μ_c/μ_d	$\eta = u_d/u_c$	Re_c	Ca_c
drop flow	1	2.39	1.07	0.0774	0.0824
jet flow	1	2.39	0.915	0.1807	0.1926

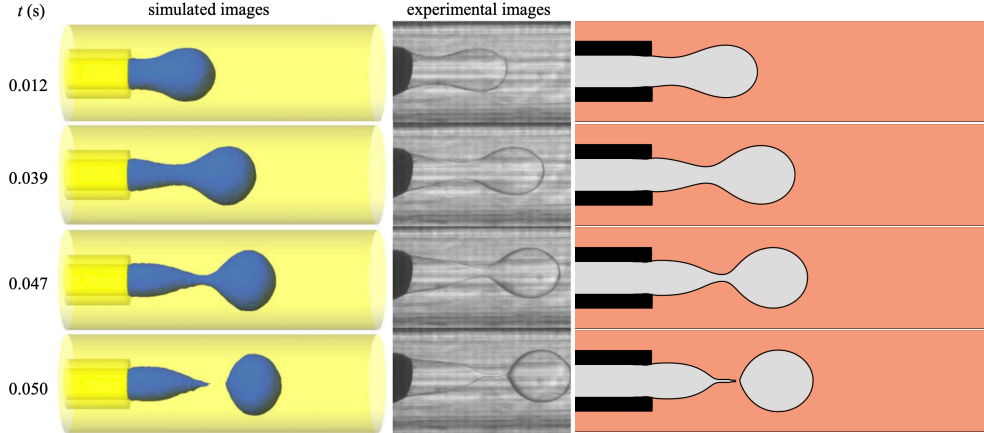
Table 2: Simulation parameters.

The comparison consists in evaluating the results of Basilisk at the same simulation instants of those of [35]. Two aspects were considered to reconstruct the images: (i) since the reference zero time of the simulations in [35] are not known, we determined comparable instants starting from the droplet detachment snapshot ($t = 0.05$) and proceeding backward; (ii) given the geometric symmetries, the simulations in Basilisk were performed considering only the upper half of the channels, and imposing axial symmetry through basilisk *axi.h* module, which introduces a metric to take into account axial symmetry in a 2D simulation, thus reducing the computational demand. The resulting images therefore have been mirrored with respect to the longitudinal axis to allow a more accurate visual comparison. The visual comparisons are shown in Figure 4 for the dripping regime and Figure 5 for the jetting regime.

As it can be seen the matching of the whole dynamics is good: first important aspect to note is that simulations correctly reproduce the generation mechanisms. Secondly, the diameter and the pinch-off position is in agreement. As in the experimental images, at the moment of pinch-off we see the thin tip of the core filament that starts to retract, in both regimes, with an abrupt change of diameter of the tip. In the jetting regime we see that there is also a good accordance in terms of Rayleigh-Plateau instability originating the pinch-off, which can be appreciated by undulations of the interface with similar wavelength.

5.1. Grid Convergence and Adaptivity Criteria

On the two reference cases shown in the previous section, we have performed a grid convergence analysis with a focus on the refinement param-



(a) Simulation and experiments from literature. Reprinted from Chemical Engineering Science, Vol. 134, W. Lan, S. Li, G. Luo, Numerical and experimental investigation of dripping and jetting flow in a coaxial micro-channel, 76-85, Copyright 2015, with permission from Elsevier.

(b) Basilisk (present work).

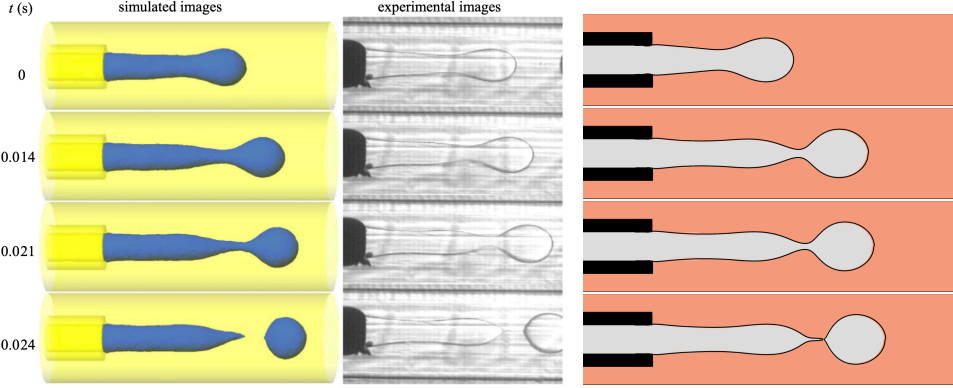
Figure 4: Droplet formation stages in the dripping regime, comparison with literature results [35]. Basilisk snapshots are at $\hat{t} = 1.72$ ($t = 0.11s$), $\hat{t} = 2.13$ ($t = 0.14s$), $\hat{t} = 2.25$ ($t = 0.148s$), $\hat{t} = 2.30$ ($t = 0.151s$).

eters. We have considered three different levels of maximum refinement, namely $LEV = 10, 11, 12$, which result in $D/\Delta = 51, 102, 204$, with the two sets of refinement parameters reported in Table 3.

	ϵ_{u_x}	ϵ_{u_y}	ϵ_{cs}	ϵ_f
base	$1.5 \cdot 10^{-2}$	$1.5 \cdot 10^{-2}$	10^{-7}	10^{-3}
ref	$1.5 \cdot 10^{-3}$	$1.5 \cdot 10^{-3}$	10^{-7}	10^{-3}

Table 3: Sets of threshold values for grid adaptivity.

For each set of refinement parameters we have carried out a grid convergence study. First of all we have evaluated the average diameter of the



(a) Simulation and experiments from literature. Reprinted from Chemical Engineering Science, Vol. 134, W. Lan, S. Li, G. Luo, Numerical and experimental investigation of dripping and jetting flow in a coaxial micro-channel, 76-85, Copyright 2015, with permission from Elsevier.

(b) Basilisk (present work).

Figure 5: Droplet formation stages in the jetting regime, comparison with literature results [35]. Basilisk snapshots are at $\hat{t} = 1.75$ ($t = 0.049s$), $\hat{t} = 2.45$ ($t = 0.063s$), $\hat{t} = 2.50$ ($t = 0.070s$), $\hat{t} = 2.60$ ($t = 0.073s$).

formed droplet and the generation frequency. For the evaluation of droplet diameter we have used basilisk *tag* function, which allows to identify each closed region of the dispersed phase with a tag, we have calculated the area of each droplet, and the resulting equivalent diameter as:

$$d_{eq} = 2\sqrt{\frac{2A_{drop}}{\pi}}. \quad (10)$$

The average diameter has been calculated by averaging over all droplets present in the domain, starting from the dimensionless time $\hat{t} = 5$. The average generation frequency is evaluated by simply counting the number of droplet generated from the first pinch-off up to the dimensionless time $\hat{t} = 20$. Results, reported in Table 4, show that if the primary interest is

on the evaluation of the regime of formation and on the average diameter and production rate, simulations with a maximum level of refinement of $LEV = 11$ with the *base* adaptivity set can be considered well converged. $LEV = 10$ with the *ref* adaptivity set is fine for the two cases analyzed here, but as it was shown in section § 4, a maximum refinement of $H/\Delta \approx 50$ is not sufficient at small Capillary numbers. Therefore $LEV = 11$ with the *base* adaptivity set is the best trade-off between accuracy and computational times.

case	dripping		jetting	
	D_{drop}/D_{duct}	$f_{pinch-off}[s^{-1}]$	D_{drop}/D_{duct}	$f_{pinch-off}[s^{-1}]$
lev11-base	0.6324	9.23	0.524	32.96
lev10-ref	0.6362	9.11	0.527	30.11
lev11-ref	0.6357	9.12	0.530	30.11
lev12-ref	0.6325	9.37	0.530	30.11

Table 4: Average diameter and pinch-off frequency of the generated droplets in the two reference simulations. The left column denotes the combination of maximum level of refinement and adaptivity threshold set.

For the sake of completeness we show in Figure 6 the time evolution of the jet length. Every jump corresponds to a pinch-off event and every minimum is the position of the jet immediately after pinch-off and eventual retraction of the tip. As expected, in the dripping regime, Figure 6(a), the break-up position is stable, while in the jetting regime, Figure 6(b), it gradually drifts downstream, and even tiny deviations of the pinchoff position at each cycle of formation sum-up and results in unmatched positions with different grids at long times when the adaptivity threshold is modified, while changing only the

maximum level of refinement maintains an excellent convergence, see Figure 6(b). In the following, however, we will focus solely on the prediction of droplet formation regimes and diameter, and only the trend of the pinch-off position will be used to classify the regime, which remains consistent across all the tested grids.

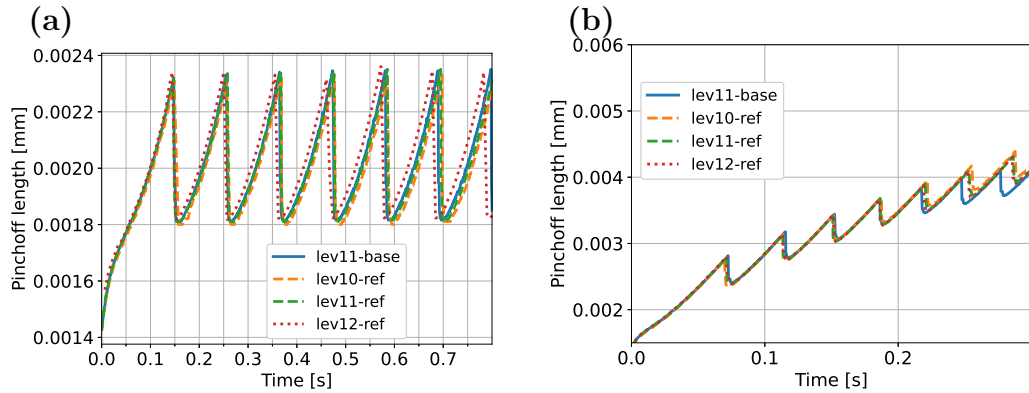


Figure 6: Thread length: minima represents pinchoff position. (a): dripping case. (b): jetting case. Evaluation of different maximum level of refinement and different adaptivity threshold criteria.

5.2. Regime maps

In this section we evaluate how the regime of droplet formation changes with respect to physical parameters and flow rates. We have performed a systematic parametric study structured in 4 campaigns of simulations, as reported below:

1. continuous phase: SO50; dispersed phase PSF 6% ($\mu_d = 9.23$);
2. continuous phase: SO50; dispersed phase PSF 8% ($\mu_d = 22.7$);
3. continuous phase: SO50; dispersed phase PSF 10% ($\mu_d = 46.2$);
4. continuous phase: SO100; dispersed phase PSF 8% ($\mu_d = 22.7$);

In such way we can appreciate variations of dispersed phase properties in campaigns 1 to 3, while in campaigns 2 and 4 we keep fixed the dispersed phase properties and we vary the continuous ones. For each campaign we have carried out $O(40)$ simulations, varying the inlet velocities of the two phases, with $u_c \in [1; 4; 6; 9; 11; 14; 16; 19; 21] \text{ mm/s}$, $u_d \in [4; 6; 8; 10; 13] \text{ mm/s}$. In Figure 7 we show the results of the 4 campaigns of simulations, in which we have identified the regimes of droplet generation in terms of Capillary number of the continuous phase and Weber number of the dispersed phase. We identify the different regimes with the following criteria: i) squeezing, when the interface reaches the wall of the duct and the volume of the formed droplet is greater than the maximum volume of a spherical droplet fitting the duct; ii) dripping when the pinch-off is stable in time and occurs always at the same position; iii) jetting, when the pinch-off position drifts downstream in time.

The black lines in Figure 7 denotes the transition zones found in the experimental work of Utada *et al.* [36], namely jet thinning, at low Weber numbers, with increasing Capillary numbers, and jet thickening, at low Capillary numbers and increasing Weber numbers. It is worth noting that in [36], although they vary the viscosity ratio in the range $\mu_d/\mu_c = 0.01 - 10$, the jet thinning transition has mostly been studied only for viscosity ratios in the lower end of the range. Our results focus on the jet thinning transition and show that the transition is strongly affected at least by the viscosity ratio of the two phases. The first noticeable result is that increasing the viscosity ratio, i.e. from $\mu_d/\mu_c = 0.18$ up to $\mu_d/\mu_c = 0.92$, keeping fixed the continuous phase viscosity (*SO50*), anticipates the transition at smaller Capillary num-

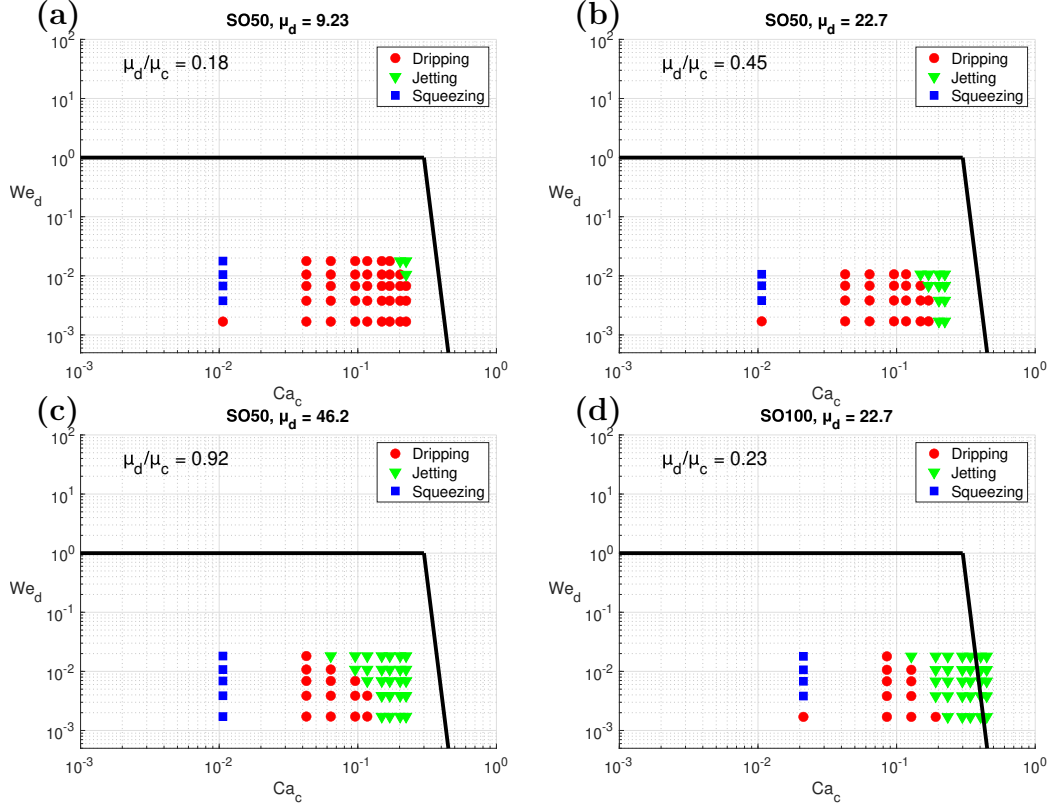


Figure 7: Maps of droplet generation regimes as a function of Ca_c and We_d . Blue squares denotes squeezing, red circles dripping, and green triangles jetting. Black lines are the transition zones of Utada *et al.* [36] Fig. 4. Each panel represents a different campaign of simulations.

bers. At the same time, we can also see from the comparison of campaigns 1) and 4), which are at similar viscosity ratios, that the transition zone is remarkably different. Keeping in mind the definition of $We_d = Re_d \cdot Ca_d$, and that the other dimensionless groups are fixed (Ca_c , μ_d/μ_c , u_d/u_c), it indicates that it is likely to be linked to the separate effect of Re_d or Ca_d . Indeed, as we can see from Figure 8, mapping the regimes in terms of the two Capillary numbers leads to a better overlap of the transition line. It implicitly means also that the dependence on Re_d is slight. Results are in

good qualitative agreement with the experimental map in [35].

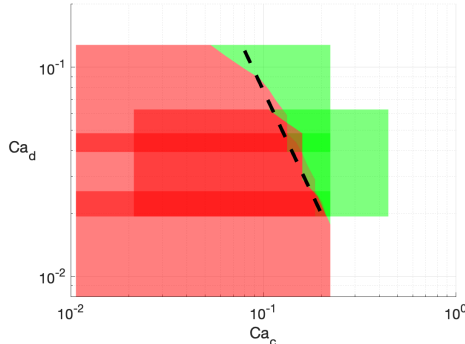


Figure 8: Maps of droplet generation regimes as a function of Ca_c and Ca_d . Red areas denote dripping, green areas denote jetting. Each box represents a different campaign of simulations.

From a more physical point of view, increasing the continuous phase Capillary number Ca_c , indeed means that the external shear increases with respect to surface tension, which results in a decrease of droplet diameters in the dripping regime, since the marginal stability is met before, at smaller diameters. The diameter reduces down to the tip diameter, then the flow transitions to jetting [36].

5.3. Droplet diameters and scaling laws

In this section we show how droplet diameters change with respect to the dimensionless numbers and the relative physical implications. The methodology for the evaluation of droplet diameters is the same used in Section 5.1. As standard, we have considered for all the simulations the diameter of the second generated droplet immediately after the pinch-off. In Figure 9 we show the variations of the droplet diameters with respect to the Capillary numbers of the two phases for two different values of the dispersed phase

viscosity (or of the viscosity ratio, since the viscosity of the continuous phase is fixed). First of all, from a qualitative point of view, we see that increasing the Capillary number of the continuous phase results in a decrease of the droplet diameter, which is straightforward since it is related to an increase of the viscous external forces on the droplet, that are destabilizing, with respect to surface tension, that is stabilizing. Therefore the marginal stability condition occurs before, i.e. at smaller diameters of the tip.

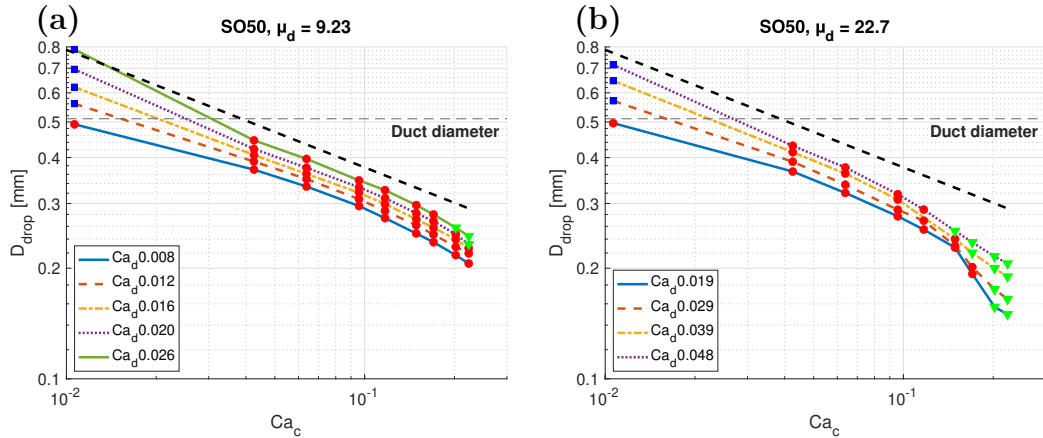


Figure 9: Diameter of the generated droplets for the campaigns 1) panel(a) and 2) panel(b). Each line corresponds to a different value of Ca_d . Blue squares are for droplet in the squeezing regime, red circles for dripping and green triangles for jetting. The dashed black line indicates the slope of -0.32 .

Variations of the Capillary number of the dispersed phase, keeping both Ca_c and μ_d/μ_c fixed, can be thought as variations of the velocity ratio, i.e.:

$$Ca_d = \frac{\mu_d u_d}{\sigma} = \frac{\mu_c u_c}{\sigma} \frac{\mu_d}{\mu_c} \frac{u_d}{u_c}. \quad (11)$$

Therefore, it is again physically consistent that increasing Ca_d results in bigger droplet diameters, due to an increased flow rate of the dispersed phase that contributes to a greater supply during the growing phase. Finally, concerning the effect of viscosities, we see from Figure 9 how increasing the

viscosity ratio μ_d/μ_c slightly decreases droplet diameters, which is due to an increased resistance to the passage of the dispersed phase through the neck. If we focus on the dripping regime (red circles in the Figure), we can see that the scaling with respect to Ca_c is consistent with the power-law $d_{drop} \propto Ca_c^{-0.34}$ proposed in [35]. However, as stated above, a dependence on the dispersed phase Capillary number and on the viscosity ratio should also be taken into account. Moreover the scaling fits well at low Capillary numbers, but deviates at the larger ones where the regime begins to transition to jetting.

Based on these evidences we sought for scaling laws that could be used to accurately predict droplet diameters in the dripping and jetting regimes, that, if combined with the regime maps of section 5.2, can help devising efficient microfluidic devices. In the dripping regime Lan *et al.* [35] have proposed a scaling law based on the continuous phase Capillary number and the dispersed phase Reynolds number, i.e. $d_{drop}/d_{in} \propto Ca_c^{-0.34} Re_d^{0.06}$. Indeed, as pointed out in the analysis of the regime maps in terms of Weber number or Capillary number, we expect a small effect of Re_d on the dynamics and on the size of the droplets, and this is confirmed by the small exponent that they found in the above relation based on their experimental results. Starting from this consideration, and following the criteria found in the analysis of regime maps and droplet diameters, we sought for a dependence of the droplet diameter of this kind: $d_{drop}/D = f(Ca_c, Ca_d, \mu_d/\mu_c, Re_d)$. We have done a linear regression to find the power-law exponents considering all simulation from all the campaigns that belong to the dripping regime, which has lead

to the following expression:

$$\frac{d_{drop}}{D} = 0.233 \cdot Ca_c^{-0.33} \cdot Ca_d^{0.2} \cdot \left(\frac{\mu_d}{\mu_c}\right)^{-0.22} \cdot Re_d^{-0.002}. \quad (12)$$

The dependence on Ca_c and the negligible effect of Re_d are in very close agreement with [35], while the additional dependence on Ca_d and μ_d/μ_c show significant exponents. Figure 10(a) shows the correlations between simulations and the above semi-empirical relation with an R^2 correlation coefficient of $R^2 = 0.96$.

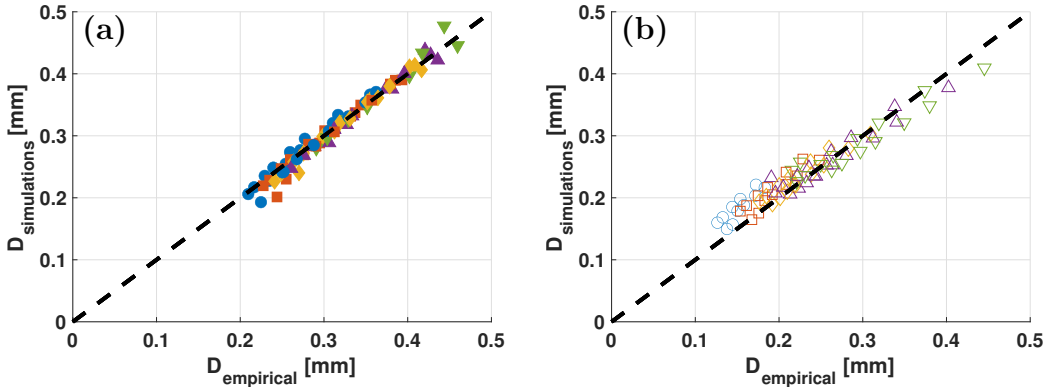


Figure 10: Correlations between droplet diameters from simulations and from semi-empirical relations Eq. 12. (a): dripping regime; (b): jetting regime. Different symbols corresponds to different values of u_d : $u_d = 4$ (blue circle), $u_d = 6$ (red square), $u_d = 8$ (yellow diamond), $u_d = 10$ (upward purple triangle), $u_d = 13$ (downward green triangle).

Concerning the scaling for the jetting regime, we started from the theoretical arguments and experimental evidences of Utada *et al.* [36] and Lan *et al.* [35] that consolidate that within the Rayleigh-Plateau instability the droplet diameter is proportional to the diameter of the jet, which is due to the fact that the most unstable mode wavelength is proportional to the jet diameter, and that the volume of the forming droplet can be considered equal to the volume contained in one wavelength [36], therefore $d_{drop} \simeq 2d_{jet}$. At the same

time, under the assumption of a Stokes flow, the diameter of a co-flowing jet can be expressed in terms of the flow rate ratio $2(d_{jet}/D)^2 \simeq Q_d/(Q_c+Q_d)$, at leading order. Based on this theoretical relation, we seek for a dependence of this kind with an additional effect of the viscosity ratio, as is evident from the above analysis. The result of a linear regression with imposed dependence on the flow rate ratio, i.e. imposing $d_{drop}/D = C \cdot [2Q_d/(Q_c + Q_d)]^{0.5} \cdot (\mu_d/\mu_c)^\alpha$, yields:

$$d_{drop}/D = 2.48 \cdot \left(\frac{Q_d}{(Q_c + Q_d)/2} \right)^{0.5} \cdot \left(\frac{\mu_d}{\mu_c} \right)^{0.124}. \quad (13)$$

Figure 10(b) shows the correlations between simulations and the above relation, which gives an R^2 correlation coefficient of $R^2 = 0.91$.

6. Discussion and Conclusions

In this work we have analyzed the suitability of the open-source software Basilisk to reproduce micro droplet generation mechanisms in micro/milli-fluidic devices. We have assessed the accuracy and the usability of Basilisk starting from the analysis of the Taylor bubble configuration, where we have found excellent agreement with theoretical and empirical literature laws for droplet terminal velocity, analyzing also the sensitivity to the main numerical parameters. We have then focused on axially-symmetric configurations, first of all replying the experimental results of Lan *et al.* [35] in the two notable regimes of dripping and jetting. Secondly, we evaluated how physical parameters affects the regimes of droplet formations and the associated diameters, via a set of 4 distinct campaigns, each one with fixed viscosity and density of the two phases, varying the inlet velocities. In such way it has been possible to map the regimes of droplet generation, at first in terms of Ca_c and We_d ,

then more effectively in terms of Ca_c and Ca_d , finding a distinct separation zone from the dripping to the jetting regime that overlap consistently for the 4 campaigns of simulations. For these campaigns of simulations we have also analyzed in details the size of the generated droplets and how they vary with respect to physical parameters, quantifying the decrease with increasing continuous phase Capillary number and with increasing dispersed phase Capillary number, in the dripping regime, and assessing the relevant dependence on the viscosity ratio in both regimes. Semi-empirical scaling laws have then been proposed for the two regimes, based on these new findings and inspired to previous literature works [35, 36].

Results on regime maps, obtained from a systematic study, support and complement literature results and can be of valuable importance for preliminary design of microfluidic coaxial devices. Similar analysis can then be extended to different layouts and configurations. Moreover the semi-empirical scaling laws of droplet diameters can be opportunely used in the search for an optimal balance between production rates and droplet size. Beyond providing quantitative results and laws that may be of practical relevance, as explained above, we have further investigated the physical reasons behind these mechanisms, emphasizing the importance of taking the viscosity ratio into account.

This work also paves the way for the use of Basilisk software in this type of microfluidic applications, thus making it possible to take advantage of its high accuracy, resulting from the sharp treatment of the interfaces, together with the benefits provided by the use of adaptive grids. Fully 3-dimensional simulations, also with more complex geometries, that will overcome the ac-

tual limitation of the combined use of the embedded framework with contact angle dynamics only in 2-dimensions, will soon be possible thanks to the continuous development and improvement of the existing functions and solvers (see Tavares *et al.* [29] for recent developments on contact angle dynamics).

Acknowledgments

This work is supported by PNRR M4C2 - HPC, Big data and Quantum Computing (Simulazioni, calcolo e analisi dei dati e altre prestazioni - CN1) - CUP I53C22000690001 SPOKE 6 Multiscale modeling & Engineering applications. We also acknowledge the CINECA award under the ISCRA initiative for the availability of high performance computing resources and support.

References

- [1] Ava M Vargason, Aaron C Anselmo, and Samir Mitragotri. The evolution of commercial drug delivery technologies. *Nature Biomedical Engineering*, 5(9):951–967, 2021.
- [2] Sarah Köster, Francesco E Angile, Honey Duan, Jeremy J Agresti, Anton Wintner, Christian Schmitz, Amy C Rowat, Christoph A Merten, Dario Pisignano, Andrew D Griffiths, et al. Drop-based microfluidic devices for encapsulation of single cells. *Lab on a Chip*, 8(7):1110–1115, 2008.
- [3] Shelley Lynn Anna. Droplets and bubbles in microfluidic devices. *Annual Review of Fluid Mechanics*, 48(1):285–309, 2016.
- [4] Taotao Fu, Yining Wu, Youguang Ma, and Huai Z Li. Droplet formation and breakup dynamics in microfluidic flow-focusing devices: From dripping to jetting. *Chemical Engineering Science*, 84:207–217, 2012.
- [5] Piotr Garstecki, Howard A Stone, and George M Whitesides. Mechanism for flow-rate controlled breakup in confined geometries: A route to monodisperse emulsions. *Physical Review Letters*, 94(16):164501, 2005.
- [6] Thomas Cubaud and Thomas G Mason. Capillary threads and viscous droplets in square microchannels. *Physics of Fluids*, 20(5), 2008.
- [7] Jinsong Hua, Baili Zhang, and Jing Lou. Numerical simulation of microdroplet formation in coflowing immiscible liquids. *AIChE Journal*, 53(10):2534–2548, 2007.

- [8] Salih Ozen Unverdi and Grétar Tryggvason. A front-tracking method for viscous, incompressible, multi-fluid flows. *Journal of Computational Physics*, 100(1):25–37, 1992.
- [9] M De Menech, Piotr Garstecki, F Jousse, and Howard A Stone. Transition from squeezing to dripping in a microfluidic T-shaped junction. *Journal of Fluid Mechanics*, 595:141–161, 2008.
- [10] Long Wu, Michihisa Tsutahara, Lae Sung Kim, and ManYeong Ha. Three-dimensional lattice Boltzmann simulations of droplet formation in a cross-junction microchannel. *International Journal of Multiphase Flow*, 34(9):852–864, 2008.
- [11] Shahriar Afkhami, Alex M Leshansky, and Yuriko Renardy. Numerical investigation of elongated drops in a microfluidic T-junction. *Physics of Fluids*, 23(2), 2011.
- [12] Shahriar Afkhami and Yuriko Renardy. A volume-of-fluid formulation for the study of co-flowing fluids governed by the Hele-Shaw equations. *Physics of Fluids*, 25(8), 2013.
- [13] Wei Yu, Xiangdong Liu, Yuanjin Zhao, and Yongping Chen. Droplet generation hydrodynamics in the microfluidic cross-junction with different junction angles. *Chemical Engineering Science*, 203:259–284, 2019.
- [14] Duong A Hoang, Volkert van Steijn, Luis M Portela, Michiel T Kreutzer, and Chris R Kleijn. Modeling of low-capillary number segmented flows in microchannels using OpenFOAM. In *AIP Conference Proceedings*, volume 1479, pages 86–89. American Institute of Physics, 2012.

- [15] Duong A Hoang, Volkert van Steijn, Luis M Portela, Michiel T Kreutzer, and Chris R Kleijn. Benchmark numerical simulations of segmented two-phase flows in microchannels using the Volume of Fluid method. *Computers & Fluids*, 86:28–36, 2013.
- [16] Maryam Fatehifar, Alistair Revell, and Masoud Jabbari. Non-Newtonian droplet generation in a cross-junction microfluidic channel. *Polymers*, 13(12):1915, 2021.
- [17] Sara Tomasi Masoni, Alessandro Mariotti, Chiara Galletti, Roberto Mauri, Maria Vittoria Salvetti, and Elisabetta Brunazzi. Formation of sodium-alginate droplets in an X-microdevice: Characterization of the pinching efficiency. *Physics of Fluids*, 36(9), 2024.
- [18] David Gabriel Harispe and Pablo A Kler. Accurate numerical prototypes of microfluidic droplet generators with open source tools. *Computers & Fluids*, 281:106366, 2024.
- [19] Stéphane Popinet. An accurate adaptive solver for surface-tension-driven interfacial flows. *Journal of Computational Physics*, 228(16):5838–5866, 2009.
- [20] Stéphane Popinet. Gerris: a tree-based adaptive solver for the incompressible Euler equations in complex geometries. *Journal of Computational Physics*, 190(2):572–600, 2003.
- [21] Cyril W Hirt and Billy D Nichols. Volume of fluid (VOF) method for the dynamics of free boundaries. *Journal of Computational Physics*, 39(1):201–225, 1981.

- [22] Grétar Tryggvason, Ruben Scardovelli, and Stéphane Zaleski. *Direct Numerical Simulations of Gas–Liquid Multiphase Flows*. Cambridge University Press, 2011.
- [23] Eugenio Aulisa, Sandro Manservisi, Ruben Scardovelli, and Stephane Zaleski. Interface reconstruction with least-squares fit and split advection in three-dimensional Cartesian geometry. *Journal of Computational Physics*, 225(2):2301–2319, 2007.
- [24] Jeremiah U Brackbill, Douglas B Kothe, and Charles Zemach. A continuum method for modeling surface tension. *Journal of Computational Physics*, 100(2):335–354, 1992.
- [25] Hans Johansen and Phillip Colella. A Cartesian grid embedded boundary method for Poisson’s equation on irregular domains. *Journal of Computational Physics*, 147(1):60–85, 1998.
- [26] Peter Schwartz, Michael Barad, Phillip Colella, and Terry Ligocki. A Cartesian grid embedded boundary method for the heat equation and Poissons equation in three dimensions. *Journal of Computational Physics*, 211(2):531–550, 2006.
- [27] Arthur R Ghigo, Stéphane Popinet, and Anthony Wachs. A conservative finite volume cut-cell method on an adaptive Cartesian tree grid for moving rigid bodies in incompressible flows. 2021.
- [28] Alexandre Limare, Stéphane Popinet, Christophe Josserand, Zhonghan Xue, and A Ghigo. A hybrid level-set/embedded boundary method ap-

plied to solidification-melt problems. *Journal of Computational Physics*, 474:111829, 2023.

- [29] Mathilde Tavares, Christophe Josserand, Alexandre Limare, Jose Ma Lopez-Herrera, and Stéphane Popinet. A coupled VOF/embedded boundary method to model two-phase flows on arbitrary solid surfaces. *Computers & Fluids*, 278:106317, 2024.
- [30] Shahriar Afkhami, Stephane Zaleski, and Markus Bussmann. A mesh-dependent model for applying dynamic contact angles to VOF simulations. *Journal of Computational Physics*, 228(15):5370–5389, 2009.
- [31] Dominique Legendre and Marco Maglio. Comparison between numerical models for the simulation of moving contact lines. *Computers & Fluids*, 113:2–13, 2015.
- [32] Jose-Maria Fullana, Yue Ling, Stéphane Popinet, and Christophe Josserand. Droplet in micro-channels: A numerical approach using an adaptive two phase flow solver. In *1st Pan-American Congress on Computational Mechanics - PANACM 2015*, 2015.
- [33] Francis Patton Bretherton. The motion of long bubbles in tubes. *Journal of Fluid Mechanics*, 10(2):166–188, 1961.
- [34] Pascale Aussillous and David Quéré. Quick deposition of a fluid on the wall of a tube. *Physics of fluids*, 12(10):2367–2371, 2000.
- [35] Wenjie Lan, Shaowei Li, and Guangsheng Luo. Numerical and experimental investigation of dripping and jetting flow in a coaxial micro-channel. *Chemical Engineering Science*, 134:76–85, 2015.

[36] Andrew S Utada, Alberto Fernandez-Nieves, Howard A Stone, and David A Weitz. Dripping to jetting transitions in coflowing liquid streams. *Physical Review Letters*, 99(9):094502, 2007.